Noise reduction in car aerodynamics using a surrogate objective function and the continuous adjoint method with wall functions

E.M. Papoutsis-Kiachagias [a], N. Magoulas [a,b], J. Mueller [b], C. Othmer [b], K.C. Giannakoglou [a,*]

[a] School of Mechanical Engineering, National Technical University of Athens, Parallel CFD & Optimization Unit, Athens, Greece
[b] Volkswagen AG, CAE Methods, Group Research, Letter Box 1777, D-38436 Wolfsburg, Germany

ARTICLE INFO

ABSTRACT

The purpose of this paper is twofold. In the first part, the continuous adjoint formulation for field integral objective functions used in steady-state, incompressible aerodynamic optimization is developed. The formulation includes the full differentiation of the Spalart–Allmaras turbulence model based on wall functions. In the second part, the developed adjoint method is used for optimizing the side mirror shape of a passenger car, using volumetric B-Splines as the parameterization tool. Based on industrial experience, an appropriate, though approximate, objective function to be minimized is expressed by the integral of the squared turbulent viscosity over a volume residing next to the driver's window. It should be stressed that if the commonly used "frozen turbulence" assumption was made, by skipping the differentiation of the turbulence model, the adjoint method would not have been able to provide any kind of sensitivity derivatives, since this objective function depends exclusively upon the turbulent viscosity.

1. Introduction

In aerodynamic shape optimization problems, the adjoint method can be used to compute or approximate the gradient of the functions of interest (either objective or constraint functions), with respect to (w.r.t.) the design variables. To this end, the system of adjoint equations must be formulated by taking into consideration the governing PDEs, i.e. the flow model equations and the corresponding boundary conditions. Solving the adjoint system of equations has a computational cost comparable to that of solving the flow equations and is independent of the number of design variables.

The adjoint equations can be formulated in either continuous or discrete form. In the former, the adjoint PDEs and their boundary conditions are derived by processing the objective function augmented by the volume integrals of the state (flow) equations multiplied by the adjoint variables. The adjoint equations are then discretized and solved [1–3]. On the other hand, in the discrete adjoint method the state equations are discretized first and the discrete adjoint equations are deduced from the discretized state equations [4–6]. The present article is concerned exclusively with the continuous adjoint method.

Any comparison between the continuous and discrete adjoint methods is beyond the scope of this paper.

When dealing with turbulent flow problems, the state PDEs comprise the mean-flow and turbulence model equations. Computing accurate sensitivity derivatives requires the differentiation of all state PDEs. However, in the majority of articles based on the continuous adjoint method, it is a common practice to avoid the differentiation of turbulence models [2,3,7,8]. This simplification is often referred to as the "frozen-turbulence" assumption. The differentiation of the turbulence model equations using the continuous adjoint method was initially addressed in [9], for the low turbulence Reynolds number variant of the Spalart–Allmaras model for incompressible flows. Later on, the continuous adjoint approach to the same turbulence model for compressible flows was also presented in [10]. The linearization of the turbulence model equations using discrete adjoint is more common and can be found, among other, in [11–15]. A hybrid adjoint method, in which the continuous adjoint mean flow equations are combined with the discrete adjoint turbulence model, was presented in [16].

In [17], the continuous adjoint method was extended to cases in which the mean–flow equations are coupled with the k–ϵ turbulence model and the wall function technique. There, the introduction of the adjoint law of the wall allowed for the adjoint system of PDEs to be treated similarly to the state equations close to the solid walls. In [18], a review on continuous adjoint methods for turbulent flows, including the adjoint to the Spalart–Allmaras model with wall functions was presented, there for objective functions defined

* Corresponding author. Tel: +30 210 772 1636; fax: +30 210 772 1658.
   E-mail addresses: vaggelisp@gmail.com (E.M. Papoutsis-Kiachagias), nikolaos.magoulas@volkswagen.de (N. Magoulas), joachim.mueller7@volkswagen.de (J. Mueller), carsten.othmer@vw.com (C. Othmer), kgianna@central.ntua.gr (K.C. Giannakoglou).

as surface integrals. Here, the continuous adjoint method to the same model is extended to also cover objective functions defined as volume integrals. The cell-centered, pressure-based implementation of the Spalart–Allmaras model with wall functions as programmed in OpenFOAM© is used as the basis of the developed adjoint formulation. This summarizes the first part of this article (Sections 2–5).

In the second part, the developed adjoint method is used to compute the sensitivity derivatives of an objective function expressing the noise perceived by the driver of a passenger car. According to Proudman's model [19], the acoustic power generated by isotropic turbulence can by derived from Lighthill's Theory of Aerodynamic Noise. Proudman's formula, in turn, can be correlated to the turbulent kinetic energy and dissipation or the levels of turbulent viscosity. So, in order to capture the noise perceived by the driver, the objective function is formulated as the volume integral of the square of the turbulent viscosity over a slim domain residing next to the driver's window. Since the highest levels of turbulence appear at the lower frequencies of the energy spectrum, this is a good surrogate model for low frequency noise. In this case, if the "frozen turbulence" assumption was made, the adjoint method would not have been able to provide any kind of sensitivity information, since the objective depends exclusively on turbulence. Before applying the developed method to a real-world application, its verification is conducted on the flow around an isolated airfoil (Section 7). There, the computed sensitivities are compared to finite differences (FD) and the loss in accuracy caused by avoiding the differentiation of the law of the wall is quantified. Then, the developed adjoint approach is used to optimize the side mirror shape of a passenger car. To this end, volumetric B-Splines [20,21], are used to parameterize the side-mirror surface and handle the mesh displacement during the optimization loop. After a few optimization cycles, a considerable reduction in the objective function is achieved (Section 8).

2. State (Flow) equations

The flow model consists of the Navier–Stokes equations for incompressible flows coupled with the Spalart–Allmaras turbulence model [22]. The mean-flow equations are given by

$$R^p = -\frac{\partial v_j}{\partial x_j} = 0 \tag{1a}$$

$$R_i^v = v_j \frac{\partial v_i}{\partial x_j} - \frac{\partial \tau_{ij}}{\partial x_j} + \frac{\partial p}{\partial x_i} = 0, \quad i = 1, 2(, 3) \tag{1b}$$

where p is the static pressure divided by the constant density, v_i is the velocity component, $\tau_{ij} = (v + v_t)(\frac{\partial v_i}{\partial x_j} + \frac{\partial v_j}{\partial x_i})$ is the stress tensor, v is the constant bulk viscosity and v_t is the turbulent viscosity. In what follows, repeated indices imply summation unless stated otherwise.

The turbulence model equation reads [22],

$$R^{\widetilde{v}} = v_j \frac{\partial \widetilde{v}}{\partial x_j} - \frac{\partial}{\partial x_j}\left[\left(v + \frac{\widetilde{v}}{\sigma}\right)\frac{\partial \widetilde{v}}{\partial x_j}\right]$$

$$- \frac{c_{b2}}{\sigma}\left(\frac{\partial \widetilde{v}}{\partial x_j}\right)^2 - \widetilde{v}P + \widetilde{v}D = 0 \tag{2}$$

where $\widetilde{v}$ is the turbulence state variable. The eddy viscosity coefficient v_t is expressed in terms of $\widetilde{v}$ as follows:

$$v_t = \widetilde{v}f_{v_1}(\widetilde{v}) \tag{3}$$

The model functions and constants can be found in [22] or [9].

Special attention must be paid to the treatment of v_i and v_t over the boundary faces (index f) where the wall function technique is employed. As programmed in OpenFOAM©, wall functions are based on a single formula modeling both the inner sublayer and the logarithmic part of the turbulent boundary layer [23]

$$f_{WF} = y_P^+ - v_P^+ - e^{-\kappa B}\left[e^{\kappa v_P^+} - 1 - \kappa v_P^+ - \frac{(\kappa v_P^+)^2}{2} - \frac{(\kappa v_P^+)^3}{6}\right] = 0 \tag{4}$$

where $\kappa = 0.41, B = 5.56$ and the non-dimensional distance and velocity at the first cell-center P off the wall are

$$y_P^+ = \frac{\Delta^P v_\tau}{v}, \quad v_P^+ = \frac{|v_i|^P}{v_\tau} \tag{5}$$

Here, v_τ is the friction velocity, computed over the wall faces as

$$v_\tau^2 = -\tau_{ij}\big|^f n_j t_i^I \tag{6}$$

where n_j and t_i^I refer to the components of the unit vectors which are normal to the wall and parallel to the velocity (which is considered to be parallel to the wall) at the first cell P. In addition, in 3D simulations, the components of the third unit base vector of a local orthogonal system are defined as $t_i^{II} = e_{ijk}n_j t_k^I$.

Since $v_i^f = 0$, the viscous flux at the wall boundary face f is given by

$$-\tau_{ij}\big|^f n_j = \left(v + v_t^f\right)\frac{v_i^P}{|Pf|} \tag{7}$$

i.e. the normal velocity gradient at f is computed through a local finite-differences scheme, where $|Pf|$ is the distance of the center of the first cell P to the boundary face. However, the differentiation normal to the boundary must be avoided on the coarse meshes used in conjunction with wall functions. To this end, Eq. (7) is corrected by computing an "artificial" v_t^f, so that the wall shear stress computed by Eq. (4) and the one computed by differentiating the velocity field and multiplying by v_t^f be identical. Solving the flow equations using the wall function technique means that Eq. (4) is solved for v_τ, by also taking Eq. (5) into consideration, at each face f using the Newton–Raphson method and, then, Eq. (6) adjusts v_t^f accordingly.

Finally, the so-called Hamilton–Jacobi equation [24],

$$R^\Delta = \frac{\partial(c_j\Delta)}{\partial x_j} - \Delta\frac{\partial^2\Delta}{\partial x_j^2} = 0 \tag{8}$$

where $c_j = \partial\Delta/\partial x_j$, is solved to provide the distance to the wall field, Δ, at all interior cell-centers.

3. A general objective function

A general objective function F consisting of a volume integral (such as the one used in Section 6) can be expressed as

$$F = \int_\Omega F_\Omega d\Omega \tag{9}$$

where Ω is the computational domain. The continuous adjoint method, including the adjoint wall functions technique, for objective functions defined as integrals over the boundary S of the computational domain is presented in detail in [18] and will not be discussed herein.

Differentiating F w.r.t. the design variables $b_n, n \in [1, N]$, after taking into consideration the Leibniz theorem for volume integrals with variable boundaries, yields

$$\frac{\delta F}{\delta b_n} = \int_\Omega \frac{\partial F_\Omega}{\partial b_n}d\Omega + \int_S F_\Omega n_k \frac{\delta x_k}{\delta b_n}dS \tag{10}$$

In Eq. (10), the symbol $\delta(\cdot)/\delta b_n$ denotes the total (or material) derivative w.r.t. the design variables and represents the total change caused by variations in b_n. The partial derivative $\partial(\cdot)/\partial b_n$ represents the variation caused purely due to changes in the flow variables (in turn, caused by the geometry deformation) without considering space deformations. The partial and total derivatives of an arbitrary variable Φ are linked through

$$\frac{\delta\Phi}{\delta b_n} = \frac{\partial\Phi}{\partial b_n} + \frac{\partial\Phi}{\partial x_k}\frac{\delta x_k}{\delta b_n} \tag{11}$$

Eq. (11) can easily be understood through the familiar concept of material derivatives in fluid dynamics by replacing time with the design variables b_n.

Eq. (10) can further be expanded by taking into consideration the dependency of F on the flow variables,

$$\frac{\delta F}{\delta b_n} = \int_\Omega \acute{F}^v_{\Omega,i} \frac{\partial v_i}{\partial b_n} d\Omega + \int_\Omega \acute{F}^p_\Omega \frac{\partial p}{\partial b_n} d\Omega + \int_\Omega \acute{F}^{\widetilde{v}}_\Omega \frac{\partial \widetilde{v}}{\partial b_n} d\Omega$$
$$+ \int_S F_\Omega n_k \frac{\delta x_k}{\delta b_n} dS + \int_S \acute{F}^v_{S,i} \frac{\partial v_i}{\partial b_n} dS + \int_S \acute{F}^p_S \frac{\partial p}{\partial b_n} dS$$
$$+ \int_S \acute{F}^{\widetilde{v}}_S \frac{\partial \widetilde{v}}{\partial b_n} dS \tag{12}$$

where $\acute{F}^\Phi_\Omega$ includes the partial derivative $\partial F_\Omega/\partial\Phi$ plus any term that might result from the use of the Gauss divergence theorem for integrals of the form $\int_\Omega \frac{\partial}{\partial b_n}(\frac{\partial\Phi}{\partial x_j})d\Omega$. The last three integrals on the r.h.s. of Eq. (12) are non-zero only if F_Ω includes differential operators of the flow variables. It should be noted that since F might depend on $\widetilde{v}$ (as is the case for the objective studied in Section 6), Eq. (12) includes also integrals containing $\partial\widetilde{v}/\partial b_n$.

4. Development of the continuous adjoint method

The starting point for the derivation of the adjoint equations is the augmented objective function, defined by expanding F with the volume integral of the state equations multiplied by the corresponding adjoint variables,

$$F_{aug} = F + \int_\Omega u_i R^v_i d\Omega + \int_\Omega q R^p d\Omega + \int_\Omega \widetilde{v}_a R^{\widetilde{v}} d\Omega + \int_\Omega \Delta_a R^\Delta d\Omega \tag{13}$$

where u_i is the adjoint velocity component, q is the adjoint pressure and $\widetilde{v}_a$ is the adjoint to $\widetilde{v}$. The latter is neglected in the commonly used "frozen turbulence" assumption. In addition, following [10,18], Eq. (13) also includes the adjoint to the distance field, Δ_a. The last integral in Eq. (13) is included in order to make the final sensitivity expression independent of variations in the distance field.

By differentiating Eq. (13) w.r.t. b_n and employing the Leibniz theorem, one gets

$$\frac{\delta F_{aug}}{\delta b_n} = \frac{\delta F}{\delta b_n} + \int_\Omega u_i \frac{\partial R^v_i}{\partial b_n} d\Omega + \int_\Omega q \frac{\partial R^p}{\partial b_n} d\Omega$$
$$+ \int_\Omega \widetilde{v}_a \frac{\partial R^{\widetilde{v}}}{\partial b_n} d\Omega + \int_\Omega \Delta_a \frac{\partial R^\Delta}{\partial b_n} d\Omega$$
$$+ \int_{S_W} \left(u_i R^v_i + q R^p + \widetilde{v}_a R^{\widetilde{v}} + \Delta_a R^\Delta\right) n_k \frac{\delta x_k}{\delta b_n} dS \tag{14}$$

The partial derivatives of the mean flow, turbulence model and Hamilton–Jacobi equations are presented in detail in [9] and [18]. For the sake of completeness, however, part of the development related to the turbulence model is repeated in Appendix A.

4.1. Field adjoint equations

After taking into consideration the development presented in [9], Appendix A as well as the general expression for $\delta F/\delta b_n$, Eq. (12), the following expression for the gradient of F is obtained:

$$\frac{\delta F_{aug}}{\delta b_n} = \int_S \mathcal{BC}^u_i \frac{\partial v_i}{\partial b_n} dS + \int_S (u_j n_j + \acute{F}^p_S) \frac{\partial p}{\partial b_n} dS + \int_S \mathcal{BC}^{\widetilde{v}_a} \frac{\partial \widetilde{v}}{\partial b_n} dS$$
$$+ \int_S 2\Delta_a \frac{\partial\Delta}{\partial x_j} n_j \frac{\partial\Delta}{\partial b_n} dS - \int_S u_i n_j \frac{\partial\tau_{ij}}{\partial b_n} dS$$
$$- \int_S \widetilde{v}_a \left(v + \frac{\widetilde{v}}{\sigma}\right) \frac{\partial}{\partial b_n} \left(\frac{\partial\widetilde{v}}{\partial x_j}\right) n_j dS + \int_\Omega R^u_i \frac{\partial v_i}{\partial b_n} d\Omega$$

$$+ \int_\Omega R^q \frac{\partial p}{\partial b_n} d\Omega + \int_\Omega R^{\widetilde{v}_a} \frac{\partial \widetilde{v}}{\partial b_n} d\Omega + \int_\Omega R^{\Delta_a} \frac{\partial\Delta}{\partial b_n} d\Omega$$
$$+ \int_{S_{W_p}} (u_i R^v_i + q R^p + \widetilde{v}_a R^{\widetilde{v}} + \Delta_a R^\Delta + F_\Omega) \frac{\delta x_k}{\delta b_n} n_k dS \tag{15}$$

where

$$\mathcal{BC}^u_i = u_i v_j n_j + \tau^a_{ij} n_j - q n_i + \widetilde{v}_a \widetilde{v} \frac{\mathcal{C}_Y}{Y} e_{mjk} \frac{\partial v_k}{\partial x_j} e_{mli} n_l + \acute{F}^v_{S,i} \tag{16}$$

$$\mathcal{BC}^{\widetilde{v}_a} = \widetilde{v}_a v_j n_j + \left(v + \frac{\widetilde{v}}{\sigma}\right) \frac{\partial\widetilde{v}_a}{\partial x_j} n_j - \frac{\widetilde{v}_a}{\sigma}\left(1 + 2c_{b_2}\right) \frac{\partial\widetilde{v}}{\partial x_j} n_j + \acute{F}^{\widetilde{v}}_S \tag{17}$$

and $\tau^a_{ij} = (v + v_t)(\frac{\partial u_i}{\partial x_j} + \frac{\partial u_j}{\partial x_i})$ are the components of the adjoint stress tensor. By zeroing the multipliers of $\partial v_i/\partial b_n$, $\partial p/\partial b_n$, $\partial\widetilde{v}/\partial b_n$ and $\partial\Delta/\partial b_n$ in the volume integrals of Eq. (15), the field adjoint equations

$$R^q = -\frac{\partial u_j}{\partial x_j} + \acute{F}^p_\Omega = 0 \tag{18}$$

$$R^u_i = u_j \frac{\partial v_j}{\partial x_i} - \frac{\partial(v_j u_i)}{\partial x_j} - \frac{\partial\tau^a_{ij}}{\partial x_j} + \frac{\partial q}{\partial x_i} + \acute{F}^v_{\Omega,i}$$
$$+ \underbrace{\widetilde{v}_a \frac{\partial\widetilde{v}}{\partial x_i} - \frac{\partial}{\partial x_l}\left(\widetilde{v}_a\widetilde{v}\frac{\mathcal{C}_Y}{Y}e_{mjk}\frac{\partial v_k}{\partial x_j}e_{mli}\right)}_{termA1} = 0, \quad i = 1,2(,3) \tag{19}$$

$$R^{\widetilde{v}_a} = -\frac{\partial(v_j\widetilde{v}_a)}{\partial x_j} - \frac{\partial}{\partial x_j}\left[\left(v + \frac{\widetilde{v}}{\sigma}\right)\frac{\partial\widetilde{v}_a}{\partial x_j}\right] + \frac{1}{\sigma}\frac{\partial\widetilde{v}_a}{\partial x_j}\frac{\partial\widetilde{v}}{\partial x_j}$$
$$+ 2\frac{c_{b2}}{\sigma}\frac{\partial}{\partial x_j}\left(\widetilde{v}_a\frac{\partial\widetilde{v}}{\partial x_j}\right) + \widetilde{v}_a\widetilde{v}\mathcal{C}_{\widetilde{v}} + \underbrace{\frac{\partial v_t}{\partial\widetilde{v}}\frac{\partial u_i}{\partial x_j}\left(\frac{\partial v_i}{\partial x_j} + \frac{\partial v_j}{\partial x_i}\right)}_{P_a}$$
$$+ (-P + D)\widetilde{v}_a + \acute{F}^{\widetilde{v}}_\Omega = 0 \tag{20}$$

$$R^{\Delta_a} = -2\frac{\partial}{\partial x_j}\left(\Delta_a\frac{\partial\Delta}{\partial x_j}\right) + \widetilde{v}\widetilde{v}_a\mathcal{C}_\Delta = 0 \tag{21}$$

are derived. Eq. (18) is the adjoint continuity equation which is not affected by the differentiation of the turbulence model. The adjoint momentum equation, Eqs. (19), includes terms resulting from the differentiation of the turbulence model equation, marked as *termA1*. These terms depend on the adjoint turbulence variable $\widetilde{v}_a$ field, computed by solving the adjoint turbulence model PDE, Eq. (20). The latter is coupled to Eq. (19) through the adjoint turbulence production term marked as P_a. The last term in Eq. (20) summarizes the contribution of the objective function differentiation to the adjoint turbulence model and will be discussed further in Section 6. Finally, Eq. (21) is the adjoint Hamilton–Jacobi equation which is solved at a post-processing step, after solving the coupled system of Eqs. (18)–(20). More details about its derivation and the impact of distance sensitivities can be found in [18].

After satisfying the field adjoint equations, the remaining terms in Eq. (15) read

$$\frac{\delta F_{aug}}{\delta b_n} = \int_S \mathcal{BC}^u_i \frac{\partial v_i}{\partial b_n} dS + \int_S (u_j n_j + \acute{F}^p_S) \frac{\partial p}{\partial b_n} dS + \int_S \mathcal{BC}^{\widetilde{v}_a} \frac{\partial\widetilde{v}}{\partial b_n} dS$$
$$+ \int_S 2\Delta_a \frac{\partial\Delta}{\partial x_j} n_j \frac{\partial\Delta}{\partial b_n} dS - \int_S u_i n_j \frac{\partial\tau_{ij}}{\partial b_n} dS$$
$$- \int_S \widetilde{v}_a\left(v + \frac{\widetilde{v}}{\sigma}\right)\frac{\partial}{\partial b_n}\left(\frac{\partial\widetilde{v}}{\partial x_j}\right)n_j dS$$
$$+ \int_{S_{W_p}} (u_i R^v_i + q R^p + \widetilde{v}_a R^{\widetilde{v}} + \Delta_a R^\Delta + F_\Omega) \frac{\delta x_k}{\delta b_n} n_k dS \tag{22}$$

The adjoint boundary conditions are formulated by appropriately treating the surface integrals in Eq. (22), containing variations in the flow variables, Section 4.2.

4.2. Adjoint boundary conditions

4.2.1. Inlet boundaries, S_I

Along S_I, Dirichlet conditions are imposed on v_i and $\widetilde{\nu}$, so the first and third integrals in Eq. (22), written along S_I, vanish. To make Eq. (22) independent of $\partial p / \partial b_n$, $\partial \tau_{ij} / \partial b_n$ and $\frac{\partial}{\partial b_n} (\frac{\partial \widetilde{\nu}}{\partial x_j}) n_j$ along S_I, the following boundary conditions are imposed

$$u_j n_j = u_{\langle n \rangle} = -\acute{F}^p_{S_I}, \quad u^I_{\langle t \rangle} = 0, \quad u^{II}_{\langle t \rangle} = 0, \quad \widetilde{\nu}_a = 0 \tag{23}$$

where $u_{\langle n \rangle}$, $u^I_{\langle t \rangle}$ and $u^{II}_{\langle t \rangle}$ are the adjoint velocity components in the orthogonal system defined by $(\mathbf{n}, \mathbf{t^I}, \mathbf{t^{II}})$ at S_I, respectively.

4.2.2. Outlet boundaries, S_O

Zero Neumann conditions are imposed on v_i and $\widetilde{\nu}$ at S_O, along with a (zero) Dirichlet condition on p. Based on these conditions, the second and sixth integrals in Eq. (22), written along S_O, vanish. The fifth integral in Eq. (22) can be considered to be negligible by assuming a developed velocity profile at S_O.

After zeroing the multiplier of $\partial \widetilde{\nu} / \partial b_n$ in the third integral of Eq. (22), a Robin-type boundary condition for $\widetilde{\nu}_a$ is imposed

$$BC^{\widetilde{\nu}_a} = \widetilde{\nu}_a v_j n_j + \left(\nu + \frac{\widetilde{\nu}}{\sigma} \right) \frac{\partial \widetilde{\nu}_a}{\partial x_j} n_j + \acute{F}^{\widetilde{\nu}}_{S_O} = 0 \tag{24}$$

In order to make Eq. (22) independent of $\partial v_i / \partial b_n$ along S_O, its first integral must be eliminated, by satisfying

$$\mathcal{BC}^u_i = u_i v_j n_j + \tau^a_{ij} n_j - q n_i + \acute{F}^v_{S_{O,i}} + \underbrace{\widetilde{\nu}_a \widetilde{\nu} \frac{C_Y}{Y} e_{mjk} \frac{\partial v_k}{\partial x_j} e_{mli} n_l}_{termA2} = 0 \tag{25}$$

where the *termA2* results from the differentiation of the turbulence model.

In order to formulate the boundary conditions for the outlet adjoint pressure and the outlet adjoint tangential velocity, Eq. (25) is decomposed into its normal and tangential components

$$q = u_{\langle n \rangle} v_{\langle n \rangle} + 2(\nu + \nu_t) \frac{\partial u_{\langle n \rangle}}{\partial n} + \acute{F}^v_{S_{O,i}} n_i + \widetilde{\nu}_a \widetilde{\nu} \frac{C_Y}{Y} e_{mjk} \frac{\partial v_k}{\partial x_j} e_{mli} n_l n_i \tag{26}$$

$$0 = v_n u^I_{\langle t \rangle} + (\nu + \nu_t) \left(\frac{\partial u^I_{\langle t \rangle}}{\partial n} + \frac{\partial u_{\langle n \rangle}}{\partial t^I} \right) + \acute{F}^v_{S_{O,i}} t^I_i$$
$$- \widetilde{\nu}_a \widetilde{\nu} \frac{C_Y}{Y} e_{mjk} \frac{\partial v_k}{\partial x_j} e_{mzi} n_z t^I_i, \quad l = I, II \tag{27}$$

giving rise to boundary conditions for q and $u^I_{\langle t \rangle}$. Finally, a zero Neumann boundary condition is imposed on $u_{\langle n \rangle}$ in order to "close" the adjoint system.

4.2.3. Fixed (S_W) and controlled (S_{W_p}) wall boundaries

Along S_W, due to the Dirichlet condition imposed on $\widetilde{\nu}$, the third integral in Eq. (22), vanishes. To make Eq. (22) independent of $\frac{\partial}{\partial b_n} (\frac{\partial \widetilde{\nu}}{\partial x_j}) n_j$, a zero Dirichlet condition is imposed on $\widetilde{\nu}_a$, i.e.

$$\widetilde{\nu}_a = 0 \tag{28}$$

In order to eliminate the dependency of $\delta F_{aug} / \delta b_n$ on $\partial p / \partial b_n$, the normal adjoint velocity must be equal to

$$u_{\langle n \rangle} = -\acute{F}^p_{S_W} \tag{29}$$

By further developing the first and fifth integrals in Eq. (22), a zero Dirichlet condition for $u^{II}_{\langle t \rangle}$ results, i.e. $u^{II}_{\langle t \rangle} = 0$, along with the following expression for u_τ:

$$u^2_\tau = -\tau^a_{ij} n_j t^I_i = \acute{F}^v_{S_{W,i}} t^I_i \tag{30}$$

which can be characterized as the *adjoint friction velocity*. Its role is similar to that of the state friction velocity, i.e. it is used to compute

the adjoint viscous flux in order to complete the adjoint momentum equilibrium at the first cell adjacent to S_W. The adjoint friction velocity is an indispensable part of the adjoint system of equations to the Spalart–Allmaras model with wall functions since, due to the long distance between f and P, differentiating normal to the wall is prone to important errors. The implications of neglecting the *adjoint law of the wall* are discussed in Section 7.

The flow conditions along the S_W and S_{W_p} boundaries are identical. As a result, the adjoint boundary conditions along S_{W_p} are the same as those imposed along S_W. Though the process of deriving the adjoint boundary conditions along S_{W_p} and S_W are similar, there is a significant difference: since S_{W_p} may vary, the total and partial derivatives of the flow quantities are different and linked through Eq. (11). In addition, the total variations in the normal and tangent surface vectors are not zero, contributing extra terms during the formulation of the adjoint boundary conditions. These extra terms comprise the sensitivity derivatives expression given in Section 4.3.

Finally, the boundary conditions for the Δ_a field can be found in [18].

4.3. Sensitivity derivatives

After satisfying the field adjoint equations and their boundary conditions, the remaining terms comprise the sensitivity derivatives expression, which reads

$$\frac{\delta F_{aug}}{\delta b_n} = T^{WF}_{SD} + \int_{S_{W_p}} u^I_{\langle t \rangle} \frac{\partial \tau_{ij}}{\partial x_k} n_j t^I_i \frac{\delta x_k}{\delta b_n} dS + \int_{S_{W_p}} u^I_{\langle t \rangle} \tau_{ij} \frac{\delta (n_j t^I_i)}{\delta b_n} \frac{\delta x_k}{\delta b_n} dS$$

$$+ \int_{S_{W_p}} \mathcal{SD}_i v^I_{\langle t \rangle} \frac{\delta t^I_i}{\delta b_n} dS - \int_{S_{W_p}} \mathcal{SD}_i \frac{\partial v_i}{\partial x_k} \frac{\delta x_k}{\delta b_n} dS$$

$$\underbrace{- \int_{S_{W_p}} \left[\nu \frac{\partial \widetilde{\nu}_a}{\partial x_j} n_j + \acute{F}^{\widetilde{\nu}}_S \right] \frac{\partial \widetilde{\nu}}{\partial x_k} \frac{\delta x_k}{\delta b_n} dS}_{termB}$$

$$- \int_{S_{W_p}} 2 \Delta_a \frac{\partial \Delta}{\partial x_j} n_j \frac{\partial \Delta}{\partial x_k} \frac{\delta x_k}{\delta b_n} dS$$

$$+ \int_{S_{W_p}} u_{\langle n \rangle} \left(\tau_{ij} \frac{\delta (n_i n_j)}{\delta b_n} + \frac{\partial \tau_{ij}}{\partial x_k} \frac{\delta x_k}{\delta b_n} n_i n_j \right) dS$$

$$+ \int_{S_{W_p}} (u_i R^v_i + q R^p + \widetilde{\nu}_a R^{\widetilde{\nu}} + \Delta_a R^\Delta + F_\Omega) \frac{\delta x_k}{\delta b_n} n_k dS \tag{31}$$

where

$$\mathcal{SD}_i = \tau^a_{ij} n_j - q n_i + \acute{F}^v_{S_{W_p,i}} \tag{32}$$

Term T^{WF}_{SD} is obtained from the differentiation of the law of the wall, Eq. (4), and the resulting correlation between the variation of the friction velocity and the velocity magnitude and distance of the first cell off the wall; its value is expressed in terms of the tangential adjoint velocity, the friction velocity and the spatial gradient of the flow velocity at the wall. In addition, *termB* results from the differentiation of the turbulence model.

5. Implementation

The method has been implemented in OpenFOAM©. The flow equations are solved using the standard steady state incompressible OpenFOAM© solver simpleFoam, utilizing a second-order upwind scheme for the convection terms. Spatial gradients are discretized using the Green–Gauss theorem and a linear interpolation of the neighboring cell values on the mesh faces for the quantities of interest. The adjoint equations are solved using the adjoint OpenFOAM© solver developed at NTUA. The flexibility provided by OpenFOAM© and the continuous adjoint method has allowed the use of a second-order downwind scheme for the convection terms, in the case of a stable
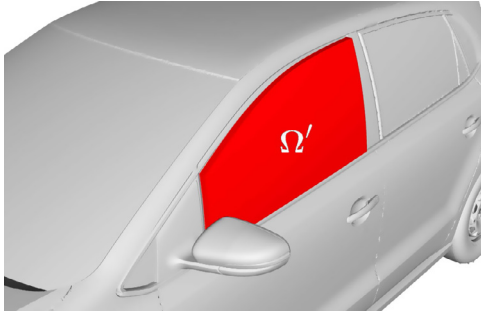
Fig. 1. Passenger car noise reduction: Ω' volume used for the definition of the surrogate noise objective function, Eq. (33). The volume has its base on the driver's window and a user-defined, finite thickness.

adjoint solution, or a first-order downwind scheme in order to improve the stability and robustness of the adjoint solution in numerically stiff industrial cases.

6. Volume integral objective function

Based on industrial experience (see comments and citation in the introduction), an objective function which is linked with the noise perceived by the driver of a car is given by

$$F = \int_{\Omega'} v_t^2 d\Omega \tag{33}$$

where Ω' is a volume residing next to the driver's window, with a user-defined thickness, Fig. 1. The differentiation of Eq. (33) yields

$$\frac{\delta F_N}{\delta b_n} = \int_{\Omega'} \underbrace{2 v_t \frac{\partial v_t}{\partial \widetilde{v}}}_{\acute{F}_\Omega^{\widetilde{v}}} \frac{\partial \widetilde{v}}{\partial b_n} d\Omega + \int_{S'} v_t^2 n_k \frac{\delta x_k}{\delta b_n} dS \tag{34}$$

Eq. (34) states that an extra source term ($\acute{F}_\Omega^{\widetilde{v}}$) must be added to the adjoint turbulence model equation, Eq. (20), in the cells contained within Ω'. This term in fact triggers the development of the adjoint flow.

7. Verification

In order to verify the adjoint formulation presented in Section 4 and its implementation, the developed code is initially verified against FD in a case concerning the flow around an isolated NACA0012 airfoil.

This symmetric airfoil is parameterized using Bézier–Bernstein polynomials with 12 control points for each of the pressure and suction sides, Fig. 2–top. A hybrid grid with 200,000 cells was used with a mean non-dimensional distance of the first cell center adjacent to the wall equal to $y^+ \approx 10$; the computational domain extends 31 chords upstream and downstream of the airfoil. The flow Reynolds number based on the airfoil chord length is $Re = 6 \times 10^6$ and the infinite flow angle is $\alpha_\infty = 3^o$. The Ω' volume used to define F is depicted in Fig. 2.

The proposed method for computing sensitivity derivatives using the adjoint wall function technique was used to obtain the sensitivities of F, defined by Eq. (33), w.r.t. the y coordinates of the control points. The outcome of this computation is compared with the result of central FD in Fig. 3–top. A step size equal to 10^{-5} was selected after conducting a study on the sensitivity of the computed FD derivatives w.r.t. the step size; the comparison showed converged values for step sizes between 10^{-5} and 10^{-6}. In Fig. 3–top, the two curves are in a good agreement, with a maximum and mean deviation of 18.8% and 9% respectively. In Fig. 3–bottom, the two aforementioned curves are also compared with the one computed by differentiating
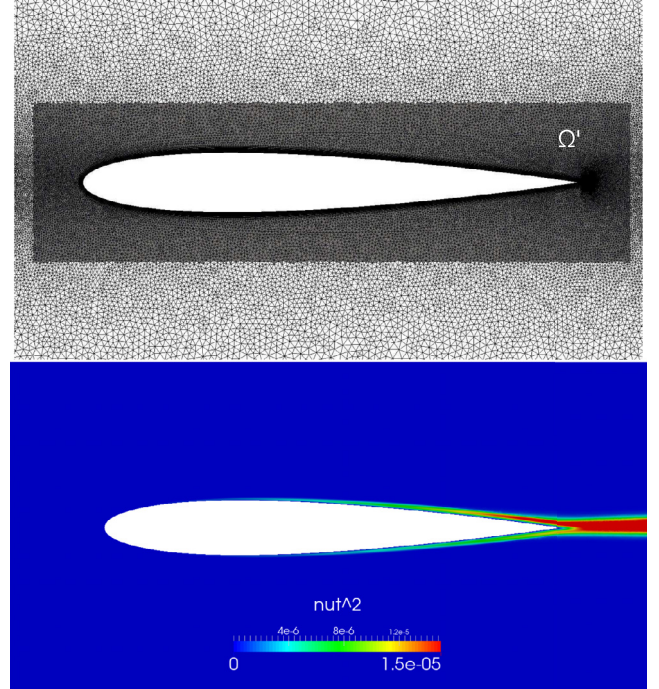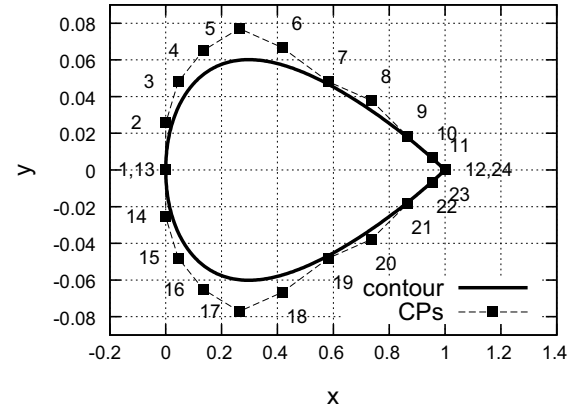

Fig. 2. NACA0012: top: airfoil contour and Bézier control points, not in scale. The leading and trailing edge control points of each side coincide. In addition, the second to last control points of each side almost coincide with the last control point, making them almost indistinguishable in this scale. Mid: a blow-up view of the mesh near the airfoil, with the volume Ω' used to define F colored in grey and residing on $x \in [-0.1, 1.1]$, $y \in [-0.16, 0.16]$. Leading and trailing edges are positioned at [0,0] and [1,0], respectively. Bottom: v_τ^2 distribution around the airfoil.

the turbulence model but disregarding the differentiation of the law of the wall. The latter implies that the solver is based on the Spalart–Allmaras model with wall functions; however, the adjoint is based on the variant of the same model in which the flow PDEs are integrated to the wall. In other words, though the turbulence model was differentiated, the law of the wall was not (no use of the adjoint law of the wall). It can be easily observed that the differentiation of the law of the wall is crucial for obtaining accurate sensitivities. At this point, it should be noted that the developed adjoint method is fully consistent with the FD scheme, as both include the differentiation of the turbulence model and the wall functions. Omitting any of them would lead to inconsistency between the adjoint and the FD methods.

8. Noise reduction on a passenger car

In the second case, the minimization of the noise perceived by the driver of a passenger car is targeted. In order to complete the
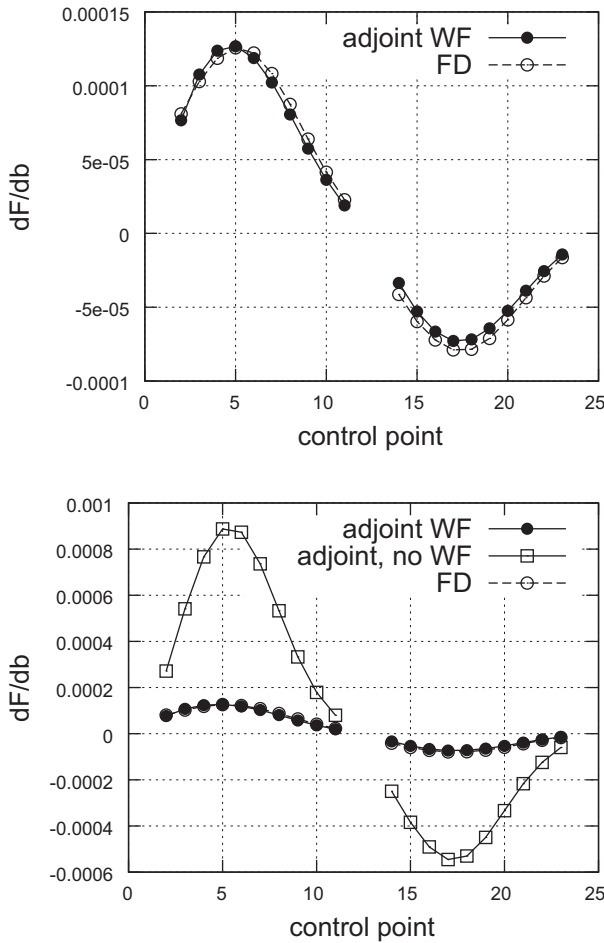
Fig. 3. NACA0012: top: sensitivities computed using the proposed method (marked as "adjoint WF") are compared to the outcome of finite differences ("FD"). The first 10 points correspond to the derivatives w.r.t. the _y_ coordinates of the Bézier–Bernstein control points parameterizing the suction side, excluding the leading and trailing edge ones, whereas the last 10 to those of the pressure side. Bottom: the above-mentioned curves are compared with the derivatives resulting from the adjoint method which includes the differentiation of the turbulence model but neglects the differentiation of the law of the wall (marked as "adjoint, no WF").
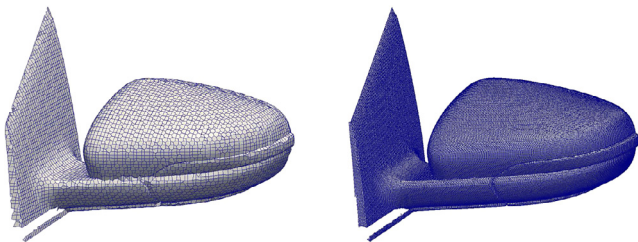
Fig. 4. Noise reduction on a passenger car: comparison of the two different mesh resolutions used for the surface mesh of the driver's mirror. Low (left) and high (right) resolution volume meshes consist of 2.4 and 30.9 million cells, respectively.

optimization at an affordable CPU cost, a relatively coarse mesh of about 2.4 million cells was used. Then, some of the geometries produced during the optimization loop were re-evaluated using a finer mesh of about 30.9 million cells, Fig. 4. For the coarse mesh, the wall clock time for computing a single flow solution on a system of 32 Intel(R) Xeon(R) CPUs E5520 @ 2.27 GHz was ∼1850 s, while the adjoint solution was obtained in ∼2650 s. For the fine mesh, the flow solution was obtained after ∼31,400 s on 128 processors of the same architecture. This considerable difference in the computational cost between the two meshes was the main reason for conducting the optimiza-
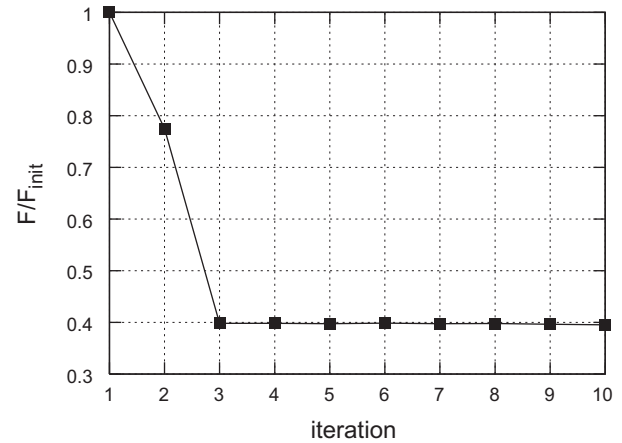

Fig. 5. Passenger car noise reduction: convergence of the objective function value for the optimization run on the coarse mesh. A 60% reduction of _F_ is observed. The total CPU time for the 10 optimization cycles was 38 h in 32 cores of 4 Intel(R) Xeon(R) E5520 @2.27 GHz CPUs.
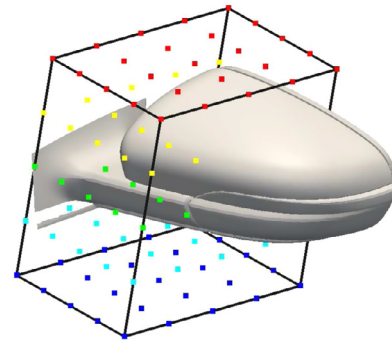

Fig. 6. Noise reduction on a passenger car: bounding box of the control points used for the volumetric B-Splines method. Control points are colored based on their _z_ coordinate. Only the internal control points were allowed to vary in the optimization loop. (For interpretation of the references to color in this figure legend, the reader is referred to the web version of this article).
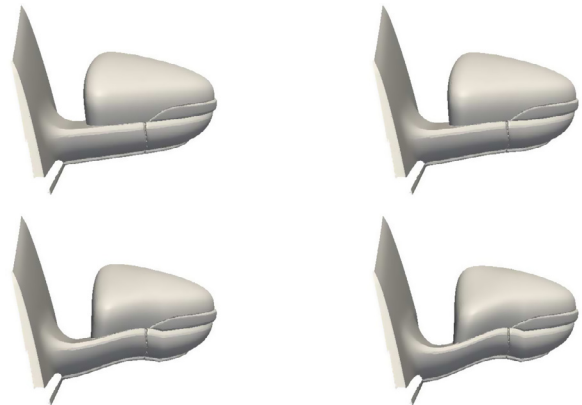

Fig. 7. Noise reduction on a passenger car: baseline (top-left) and morphed driver's mirror geometries.

tion using the coarse mesh. Mapping the geometries from the coarse to the fine mesh was facilitated by the use of volumetric B-Splines as the parameterization and mesh displacement tool. Details about this method can be found in Appendix B.

The objective function is defined on a volume Ω' next to the driver's window, as illustrated in Fig. 1. A control box with 5 control points in each direction is placed around the driver's mirror defining the volume to be morphed, Fig. 6. The position and size of the
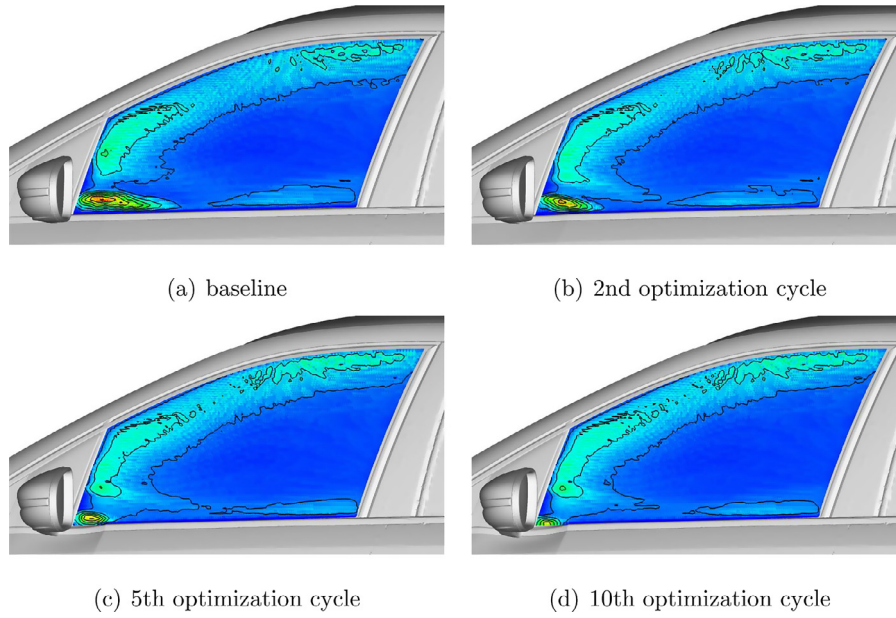
(a) baseline

(b) 2nd optimization cycle

(c) 5th optimization cycle

(d) 10th optimization cycle

Fig. 8. Noise reduction on a passenger car: v_t^2 field computed using the baseline and three morphed geometries, plotted on a plane inside the objective function volume Ω'. It can clearly be observed that the wake of the mirror has a significant contribution to the objective function value, which is reduced in the morphed geometries.
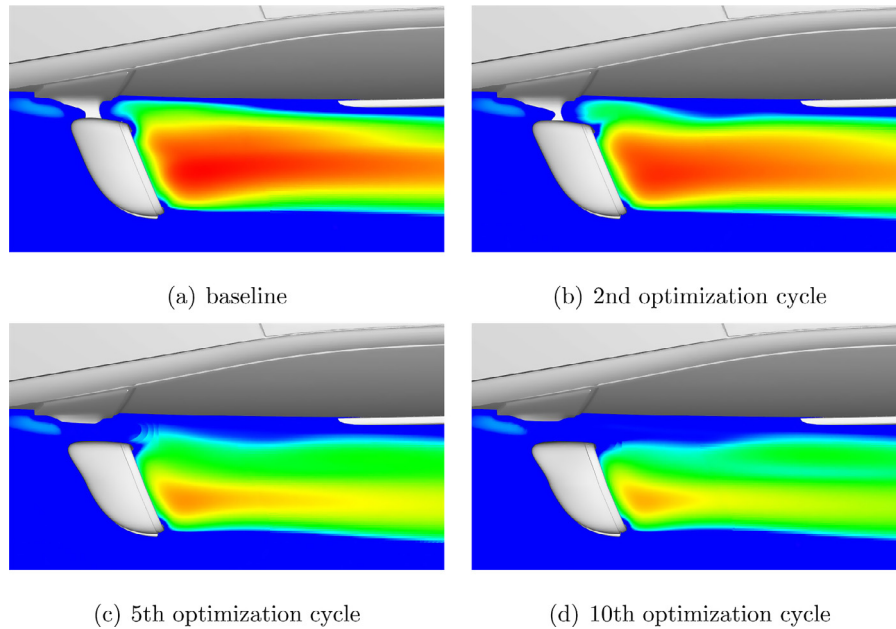

(a) baseline

(b) 2nd optimization cycle

(c) 5th optimization cycle

(d) 10th optimization cycle

Fig. 9. Passenger car noise reduction: v_t^2 field computed using the baseline and three morphed geometries, plotted on a plane parallel to the road. A significant decrease in the v_t values is observed not only close to the wall, where Ω' is located, but also along the entire length of the mirror wake.

control box was determined after having computed the adjoint surface sensitivities and locating the areas with the highest potential for optimization. The basis functions degree was set to 4 in all space directions. The boundary control points were not allowed to vary in order to prevent mesh elements from overlapping at the boundaries of the control box, giving rise to 81 design variables.

After solving the flow equations for the coarse mesh, the complete system of adjoint equations was solved, including the adjoint to the turbulence model equation and the adjoint wall functions, Sections 4.1–4.2. Subsequently the sensitivity derivatives w.r.t. the control points movement were computed and the Fletcher–Reeves conjugate gradient method [25], was used to update the design variables. At the end of each morphing, iteration the quality of the mesh was evaluated according to the standard mesh checking rou-

tines of OpenFOAM©, by monitoring the cell aspect ratio, face non-orthogonality and skewness. For all the meshes used during the optimization loop, mesh quality metrics were well above the minimum required to obtain a converged solution.

The optimization was conducted without imposing constraints and this might lead to impractical optimized shapes, such as a vanishing mirror. Alternatively, by imposing manufacturing constraints, such as a minimum mirror area or minimum mirror foot thickness, problems of this kind could be prevented. In such a case, the constraints could be handled by an optimization method based on the ALM or SQP approaches. The optimization algorithm was allowed to advance for 10 cycles, after which the results were evaluated anew on the fine mesh. The convergence of the objective function is presented in Fig. 5.
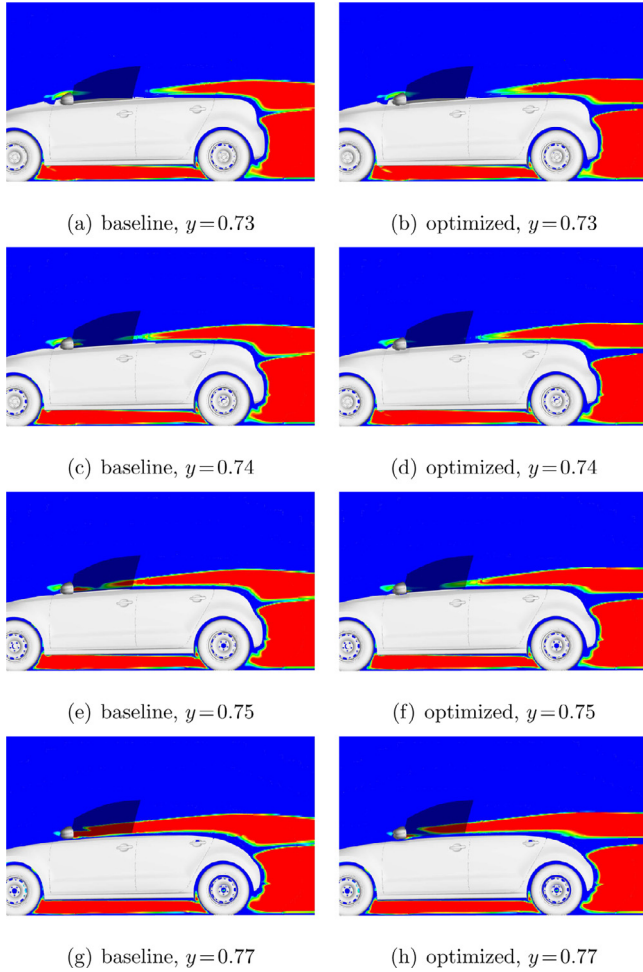
Fig. 10. Noise reduction on a passenger car: ν_t^2 field computed using the baseline (left) and the final optimized geometry (right), plotted at longitudinal planes with different y values. The shadowed area indicates the Ω' volume used to define F.

Upon the end of the optimization loop, the flow equations were solved anew for some of the geometries extracted from different optimization steps and the objective function was re-computed in order to confirm that the performance of the designed geometries was increased on the high resolution meshes as well.

Among the geometries generated through the optimization loop, the ones of steps 2, 5 and 10 were selected to be mapped and re-evaluated using the fine mesh. In Fig. 7 a comparison of the baseline and optimized geometries is presented. The objective function value for each optimized geometry is decreased by 13.8%, 23.4% and 24.6% respectively, compared to the F value computed using the baseline geometry and the same mesh resolution.

In Figs. 8–10, the ν_t^2 field around the baseline and optimized geometries are illustrated, while a similar comparison for the velocity fields is presented in Fig. 11. It can be observed that the recirculation area downstream of the mirror has been considerably reduced, leading to a local increase in the velocity magnitude (Fig. 12) and a decrease in the ν_t^2 values, reducing thus the objective function value.

9. Conclusions

The exact continuous adjoint formulation to steady-state, incompressible flows governed by the Spalart–Allmaras model with wall functions was presented. The adjoint formulation introduced the adjoint law of the wall for a cell-centered finite-volume discretization applying a no-slip velocity at the wall boundaries. The computed sensitivities resulting by the proposed formulation were verified against finite differences in an isolated airfoil case. An optimization problem based on a surrogate noise function which depends exclusively on the turbulent viscosity, integrated over a volume next to the aerodynamic body was examined. It should be noted that obtaining adjoint-based sensitivities for this function would not have been possible without differentiating the turbulence model since the acquired sensitivities would have zero values irrespective of the body shape. Thus, a clear message of the work presented in this paper is that some optimization problems cannot be solved using the adjoint method without differentiating the turbulence model. The proposed adjoint method computed accurate sensitivities, while the variant that differentiates the turbulence model without differentiating the law of the wall
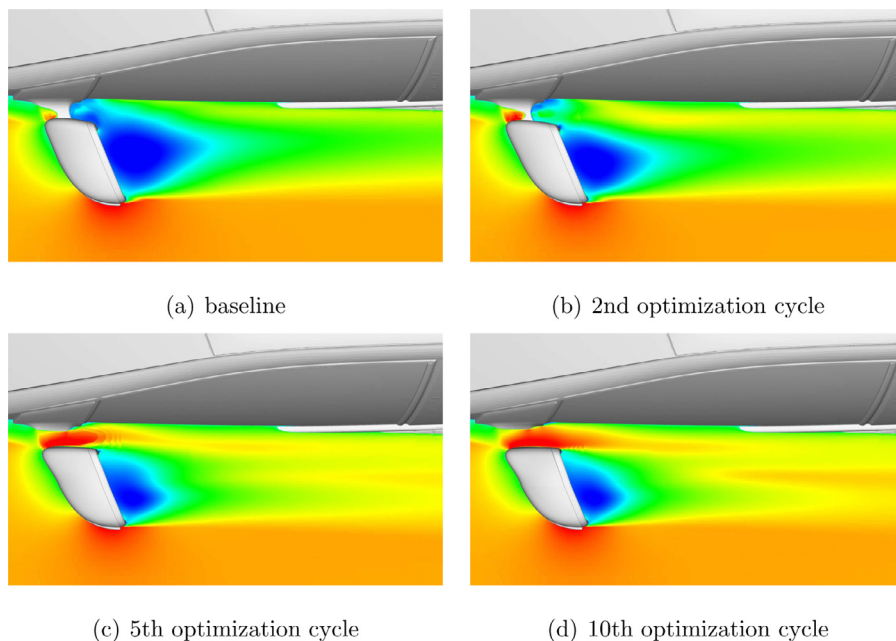

Fig. 11. Noise reduction on a passenger car: magnitude of the velocity field computed using the baseline and morphed geometries. The volume of the recirculation area close to Ω' has decreased.
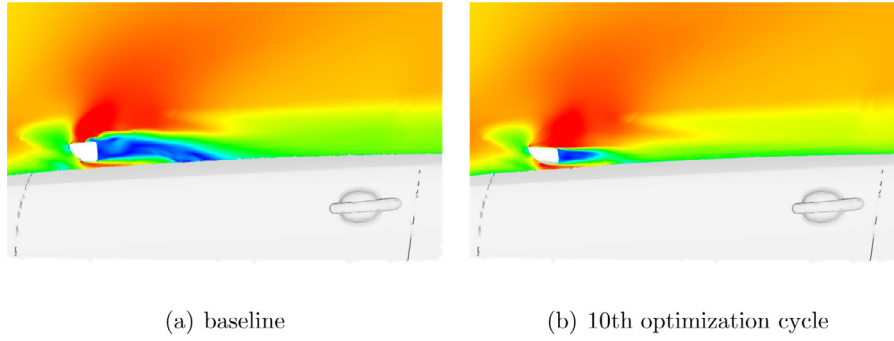
(a) baseline

(b) 10th optimization cycle

Fig. 12. Noise reduction on a passenger car: magnitude of the velocity field computed using the baseline and optimized geometries. A large part of the recirculation area behind the foot of the mirror has been suppressed and deflected away from entering the control volume next to the driver's window.

deviated from the outcome of finite differences, highlighting the necessity of using the adjoint law of the wall. The reduction of the noise perceived by the driver of a passenger car was the target of the industrial application. The developed adjoint method was coupled with a volumetric B-Splines morphing tool and supported an optimization loop in order to morph the shape of the driver's mirror. For the optimized geometry, the objective function took on a value which is lower by $\sim 25\%$ compared to that of the baseline geometry.

Acknowledgments

Appendix A. Differentiation of the mean flow and turbulence model equations

The partial derivatives of the mean-flow equations w.r.t. the design variables read

$$\frac{\partial R^p}{\partial b_n} = -\frac{\partial}{\partial x_j}\left(\frac{\partial v_j}{\partial b_n}\right) \tag{A.1}$$

$$\frac{\partial R_i^v}{\partial b_n} = \frac{\partial v_j}{\partial b_n}\frac{\partial v_i}{\partial x_j} + v_j\frac{\partial}{\partial x_j}\left(\frac{\partial v_i}{\partial b_n}\right) + \frac{\partial}{\partial x_i}\left(\frac{\partial p}{\partial b_n}\right)$$
$$- \frac{\partial}{\partial x_j}\left[\frac{\partial v_t}{\partial b_n}\left(\frac{\partial v_i}{\partial x_j} + \frac{\partial v_j}{\partial x_i}\right)\right]$$
$$- \frac{\partial}{\partial x_j}\left\{(v + v_t)\left[\frac{\partial}{\partial x_j}\left(\frac{\partial v_i}{\partial b_n}\right) + \frac{\partial}{\partial x_i}\left(\frac{\partial v_j}{\partial b_n}\right)\right]\right\} \tag{A.2}$$

After substituting Eqs. (A.1) and (A.2) into Eq. (14), the first and second integrals on the r.h.s. of the latter can be developed by using the Green–Gauss theorem. The development of the terms including the pressure and velocities variations is straightforward and can be found in [9,18]. The integral of the underlined term in Eq. (A.2) containing the variation in v_t can be developed as

$$-\int_\Omega u_i \frac{\partial}{\partial x_j}\left[\frac{\partial v_t}{\partial b_n}\left(\frac{\partial v_i}{\partial x_j} + \frac{\partial v_j}{\partial x_i}\right)\right]d\Omega$$
$$= -\int_S u_i\left(\frac{\partial v_i}{\partial x_j} + \frac{\partial v_j}{\partial x_i}\right)n_j\frac{\partial v_t}{\partial \widetilde{v}}\frac{\partial \widetilde{v}}{\partial b_n}dS$$
$$+ \int_\Omega \frac{\partial u_i}{\partial x_j}\left(\frac{\partial v_i}{\partial x_j} + \frac{\partial v_j}{\partial x_i}\right)\frac{\partial v_t}{\partial \widetilde{v}}\frac{\partial \widetilde{v}}{\partial b_n}d\Omega \tag{A.3}$$

The differentiation of the turbulence model equation, Eq. (2), gives

$$\frac{\partial R^{\widetilde{v}}}{\partial b_n} = \underbrace{\frac{\partial \widetilde{v}}{\partial x_j}\frac{\partial v_j}{\partial b_n} + v_j\frac{\partial}{\partial x_j}\left(\frac{\partial \widetilde{v}}{\partial b_n}\right)}_{g_1} - \underbrace{\frac{\partial}{\partial x_j}\left[\left(v + \frac{\widetilde{v}}{\sigma}\right)\frac{\partial}{\partial x_j}\left(\frac{\partial \widetilde{v}}{\partial b_n}\right)\right]}_{g_2}$$
$$\underbrace{-\frac{1}{\sigma}\frac{\partial}{\partial x_j}\left(\frac{\partial \widetilde{v}}{\partial b_n}\frac{\partial \widetilde{v}}{\partial x_j}\right)}_{g_3} \underbrace{-2\frac{c_{b2}}{\sigma}\frac{\partial \widetilde{v}}{\partial x_j}\frac{\partial}{\partial x_j}\left(\frac{\partial \widetilde{v}}{\partial b_n}\right)}_{g_4}$$
$$+ \underbrace{\widetilde{v}\left(-\frac{\partial P}{\partial b_n} + \frac{\partial D}{\partial b_n}\right)}_{g_5} + \underbrace{(-P + D)\frac{\partial \widetilde{v}}{\partial b_n}}_{g_6} \tag{A.4}$$

The differentiation of the production and destruction terms yields

$$-\frac{\partial P}{\partial b_n} + \frac{\partial D}{\partial b_n} = \mathcal{C}_{\widetilde{v}}\frac{\partial \widetilde{v}}{\partial b_n} + \mathcal{C}_\Delta\frac{\partial \Delta}{\partial b_n} + \mathcal{C}_Y\frac{1}{Y}e_{mjk}\frac{\partial v_k}{\partial x_j}e_{mli}\frac{\partial}{\partial x_l}\left(\frac{\partial v_i}{\partial b_n}\right) \tag{A.5}$$

where $\mathcal{C}_{\widetilde{v}}, \mathcal{C}_\Delta, \mathcal{C}_Y$ are the derived coefficients.

After substituting Eq. (A.4) into Eq. (14), the corresponding integral is expanded by using the Green–Gauss theorem. This development is presented below following a term-by-term analysis:

$$\int_\Omega \widetilde{v}_a g_1 d\Omega = \int_S \widetilde{v}_a v_j n_j \frac{\partial \widetilde{v}}{\partial b_n}dS + \int_\Omega \widetilde{v}_a \frac{\partial \widetilde{v}}{\partial x_j}\frac{\partial v_j}{\partial b_n}d\Omega$$
$$- \int_\Omega \frac{\partial(\widetilde{v}_a v_j)}{\partial x_j}\frac{\partial \widetilde{v}}{\partial b_n}d\Omega \tag{A.6}$$

$$\int_\Omega \widetilde{v}_a g_2 d\Omega = -\int_S \widetilde{v}_a n_j\left(v + \frac{\widetilde{v}}{\sigma}\right)\frac{\partial}{\partial x_j}\left(\frac{\partial \widetilde{v}}{\partial b_n}\right)dS$$
$$+ \int_S \frac{\partial \widetilde{v}_a}{\partial x_j}n_j\left(v + \frac{\widetilde{v}}{\sigma}\right)\frac{\partial \widetilde{v}}{\partial b_n}dS$$
$$- \int_\Omega \frac{\partial}{\partial x_j}\left[\left(v + \frac{\widetilde{v}}{\sigma}\right)\frac{\partial \widetilde{v}_a}{\partial x_j}\right]\frac{\partial \widetilde{v}}{\partial b_n}d\Omega \tag{A.7}$$

$$\int_\Omega \widetilde{v}_a g_3 d\Omega = -\int_S \frac{\widetilde{v}_a}{\sigma}\frac{\partial \widetilde{v}}{\partial x_j}n_j\frac{\partial \widetilde{v}}{\partial b_n}dS + \int_\Omega \frac{1}{\sigma}\frac{\partial \widetilde{v}_a}{\partial x_j}\frac{\partial \widetilde{v}}{\partial x_j}\frac{\partial \widetilde{v}}{\partial b_n}d\Omega \tag{A.8}$$

$$\int_\Omega \widetilde{v}_a g_4 d\Omega = -\int_S 2\widetilde{v}_a\frac{c_{b2}}{\sigma}\frac{\partial \widetilde{v}}{\partial x_j}n_j\frac{\partial \widetilde{v}}{\partial b_n}dS$$
$$+ \int_\Omega 2\frac{c_{b2}}{\sigma}\frac{\partial}{\partial x_j}\left[\widetilde{v}_a\frac{\partial \widetilde{v}}{\partial x_j}\right]\frac{\partial \widetilde{v}}{\partial b_n}d\Omega \tag{A.9}$$

$$\int_\Omega \widetilde{v}_a g_5 d\Omega = \int_S \widetilde{v}_a \widetilde{v}\frac{\mathcal{C}_Y}{Y}e_{mjk}\frac{\partial v_k}{\partial x_j}e_{mli}n_l\frac{\partial v_i}{\partial b_n}dS + \int_\Omega \widetilde{v}_a\widetilde{v}\mathcal{C}_{\widetilde{v}}\frac{\partial \widetilde{v}}{\partial b_n}d\Omega$$
$$+ \int_\Omega \widetilde{v}_a\widetilde{v}\mathcal{C}_\Delta\frac{\partial \Delta}{\partial b_n}d\Omega$$
$$- \int_\Omega \frac{\partial}{\partial x_l}\left(\widetilde{v}_a\widetilde{v}\frac{\mathcal{C}_Y}{Y}e_{mjk}\frac{\partial v_k}{\partial x_j}e_{mli}\right)\frac{\partial v_i}{\partial b_n}d\Omega \tag{A.10}$$

Appendix B. Volumetric B-Splines as a parameterization and mesh displacement tool

Let b_m^{ijk}, $m \in [1, 3]$, $i \in [0, I]$, $j \in [0, J]$, $k \in [0, K]$ be the Cartesian coordinates of the i, j and k-th control points of the 3D structured control grid, Fig. 6. I, J and K are the number of control points per control grid direction. The Cartesian coordinates $\mathbf{x} = [x_1, x_2, x_3]^T = [x, y, z]^T$ of a CFD mesh point residing within the boundaries defined by the control grid are given by

$$x_m(u, v, w) = U_{i,pu}(u) V_{j,pv}(v) W_{k,pw}(w) b_m^{ijk} \tag{B.1}$$

Here, $\mathbf{u} = [u_1, u_2, u_3]^T = [u, v, w]^T$ are the mesh point parametric coordinates, U, V and W are the B-Splines basis functions and pu, pv and pw their respective degrees, which may be different per control grid direction. Details about B-Splines basis definitions and properties can be found in [26]. Computing the Cartesian coordinates of any parameterized mesh point is straightforward, at a negligible computational cost, as long as its parametric coordinates $\mathbf{u}$ are known. Mesh parametric coordinates can be computed with accuracy, since a mapping from $\Re^3(x, y, z) \rightarrow \Re^3(u, v, w)$ is required. This means that volumetric B-Splines can reproduce any geometry to machine accuracy.

Given the control points position, the knot vectors and the basis functions degrees, the parametric coordinates (u, v, w) of a point with Cartesian coordinates $\mathbf{r} = [x_r, y_r, z_r]^T$ can be computed by solving the system of equations

$$\mathbf{R}(u, v, w) = \begin{bmatrix} x(u, v, w) - x_r = 0 \\ y(u, v, w) - y_r = 0 \\ z(u, v, w) - z_r = 0 \end{bmatrix} \tag{B.2}$$

where $x_m(u, v, w)$ are computed through Eq. (B.1), based on the known $\mathbf{b}$ values. The 3×3 system of Eq. (B.2) can be solved independently for each parameterized mesh point using the Newton–Raphson method, after computing and inverting the Jacobian $\partial x_m / \partial u_j$, $m, j \in [1, 3]$. The Jacobian matrix has a closed form expression resulting by differentiating Eq. (B.1) w.r.t. the components of $\mathbf{u}$. Since the evaluation of the parametric coordinates of each point is independent from any other mesh point, these computations may run efficiently in parallel.

The aforementioned process has to be done only once and can be seen as the "training phase" of the method. Then, after moving the control points $\mathbf{b}$, the Cartesian coordinates of each (internal or boundary) mesh point residing within the control grid can be computed through Eq. (B.1) at a very low cost, making volumetric B-Splines a powerful surface parameterization and mesh displacement tool. In addition, since x_m depends only on (u, v, w) (which remain unchanged whatever the change in $\mathbf{b}$ might be) and $\mathbf{b}$, the deformed meshes are step-independent. This facilitates the mapping of a geometry parameterized using volumetric B-Splines from one CFD mesh to another. Provided that the initial control grid for the two CFD meshes is the same, the control points displacement computed over the first mesh can be applied to the second too; then, the CFD mesh point positions of the second mesh can easily be computed through Eq. (B.1).

References

[1] Jameson A. Aerodynamic design via control theory. J Sci Comput 1988;3:233–60.
[2] Anderson W, Venkatakrishnan V. Aerodynamic design optimization on unstructured grids with a continuous adjoint formulation. Comput Fluids 1999;28:443–80.
[3] Papadimitriou D, Giannakoglou K. A continuous adjoint method with objective function derivatives based on boundary integrals for inviscid and viscous flows. J Comput Fluids 2007;36:325–41.
[4] Burgreen G, Baysal O. Three-dimensional aerodynamic shape optimization using discrete sensitivity analysis. AIAA J 1996;34:1761–70.
[5] Elliot J, Peraire J. Aerodynamic design using unstructured meshes. In: Proceedings of the 27th AIAA fluid dynamics conference, New Orleans, LA, paper 1996-1941; 1996.
[6] Giles M, Pierce N. Adjoint equations in CFD: duality, boundary conditions and solution behaviour. In: Proceedings of the 13th AIAA fluid dynamics conference, New Orleans, LA, paper 1997-1850; 1997.
[7] Jameson A, Pierce N, Martinelli L. Optimum aerodynamic design using the Navier–Stokes equations. Theor Comput Fluid Dyn 1998;10:213–37.
[8] Othmer C. A continuous adjoint formulation for the computation of topological and surface sensitivities of ducted flows. Int J Numer Methods Fluids 2008;58:861–77.
[9] Zymaris A, Papadimitriou D, Giannakoglou K, Othmer C. Continuous adjoint approach to the Spalart–Allmaras turbulence model for incompressible flows. Comput Fluids 2009;38:1528–38.
[10] Bueno-Orovio A, Castro C, Palacios F, ZuaZua E. Continuous adjoint approach for the Spalart–Allmaras model in aerodynamic optimization. AIAA J 2012;50:631–46.
[11] Anderson W, Bonhaus D. Airfoil design on unstructured grids for turbulent flows. AIAA J 1999;37:185–91.
[12] Nielsen E, Lu J, Park M, Darmofal D. An implicit exact dual adjoint solution method for turbulent flows on unstructured grids. Comput Fluids 2004;33:1131–55.
[13] Lee B, Kim C. Automated design methodology of turbulent internal flow using discrete adjoint formulation. Aerosp Sci Technol 2007;11:163–73.
[14] Dwight R, Brezillon J, Vollmer D. Efficient algorithms for solution of the adjoint compressible Navier–Stokes equations with applications. In: Proceedings of the ONERA-DLR aerospace symposium (ODAS), Toulouse; 2006.
[15] Marta A, Shankaran S. On the handling of turbulence equations in RANS adjoint solvers. Comput Fluids 2013;74:102–13.
[16] Taylor T, Palacios F, Duraisami K, Alonso J. A hybrid adjoint approach applied to turbulent flow simulations. In: Proceedings of the 21st AIAA computational fluid dynamics conference, San Diego, California, paper 2013-2452; 2013.
[17] Zymaris A, Papadimitriou D, Giannakoglou K, Othmer C. Adjoint wall functions: a new concept for use in aerodynamic shape optimization. J Comput Phys 2010;229:5228–45.
[18] Papoutsis-Kiachagias E, Giannakoglou K. Continuous adjoint methods for turbulent flows, applied to shape and topology optimization: industrial applications. Arch Comput Methods Eng 2014;21:1–45.
[19] Proudman I. The generation of noise by isotropic turbulence. Proc R Soc A 1952;214:119–32.
[20] Gangon H, Zingg D. Two-level free-form deformation for high-fidelity aerodynamic shape optimization. In: Proceedings of the 12th AIAA Aviation technology, integration, and operations (ATIO) conference, Indianapolis, Indiana, paper 2012-5447; 2012.
[21] Martin MJ, Andres E, Lozano C, Valero E. Volumetric B-splines shape parametrization for aerodynamic shape design. Aerosp Sci Technol 2014;37:26–36.
[22] Spalart P, Allmaras S. A one-equation turbulence model for aerodynamic flows. In: Proceedings of the 30th AIAA aerospace sciences meeting and exhibit, Reno, Nevada, paper 1992-0439; 1992.
[23] Frink N. Assessment of an unstructured-grid method for predicting 3-D turbulent viscous flows. In: Proceedings of the 34th AIAA aerospace sciences meeting and exhibit, paper 1996-0292. Reno, Nevada; 1996.
[24] Tucker P. Differential equation-based wall distance computation for DES and RANS. J Comput Phys 2003;190:229–48.
[25] Fletcher R, Reeves CM. Function minimization by conjugate gradients. Comput J 1964;7:149–54.
[26] Piegl L, Tiller W. The NURBS book. Springer; 1997.